Supporting Information

Green reconstruction of MIL-100 (Fe) in water for high crystallinity and enhanced guest encapsulation

Barbara E. Souza,[a] Annika F. Möslein,[a] Kirill Titov,[a] James D. Taylor,[b] Svemir Rudić,[b] and Jin-Chong Tan[a]*

[a] Multifunctional Materials & Composites (MMC) Lab, Department of Engineering Science, University of Oxford, Parks Road, Oxford OX1 3PJ, UK

[b] STFC Rutherford Appleton Laboratory, ISIS Neutron and Muon Source, Chilton, Didcot OX11 0QX, UK
*J.C. Tan, email: jin-chong.tan@eng.ox.ac.uk

Table of Contents

1. Materials synthesis

1.1. Mechanochemistry of MIL-100 and crystallinity reconstruction

The MIL-100 (Fe) MOF material was synthesized *via* a manual grinding-annealing process. $Fe(NO_3)\cdot 9H_2O$ [iron(III) nitrate 9-hydrate] (3 mmol) with H_3BTC [benzene-1,3,5-tricarboxilic acid] (2 mmol) were combined in the agate mortar and manually ground for 10 min. The resulting material was heated in the oven at 160 °C for 4 h to complete the annealing process. The product was washed by centrifugation (8000 rpm for 10 min) with methanol and deionized water to remove any unreacted components. Pristine MIL-100 (Fe) was then dried at room temperature and activated under vacuum at 150 °C for 12 h.

To perform the reconstruction and crystallinity studies, MIL-100 (Fe) particles were immersed into deionized water and kept under stirring at room temperature. After different immersion times, the samples were separated by centrifugation (8000 rpm for 10 min) and the supernatant was collected to measure the pH values of the reconstruction solution. Finally, the recovered MIL-100 (Fe) samples were dried at room temperature and re-activated under vacuum at 150 °C for 12 h. The reconstruction process was repeated to ensure reproducibility of results acquired with reconstruction and the product obtained *via* the manual grinding method.

1.2. Drug@MIL-100 composite systems preparation

The drug@MOF systems were synthesized as follows. Encapsulation during the reconstruction process was performed by immersion of pre-activated MIL-100 (Fe) samples in a saturated aqueous drug solution (*i.e.* 12 mg/ml for 5-FU, 20 mg/ml for caffeine, and 3.3 mg/ml for aspirin) under continuous stirring for different time periods at room temperature. The drug-loaded drug@MIL-100_REC particles were separated by centrifugation (8000 rpm for 10 min) and then activated at 130 °C for 12 h in a vacuum oven.

Table S1: Samples description and details

	Samples	**Synthesis method**	**Details**
Reconstruction studies	MIL-100 (Fe)	Manual grinding	-
	MIL-100 (Fe) Day x [a]		Samples collected after different x immersion times
Encapsulation during reconstruction	5-FU@MIL-100_REC	Manual grinding (reconstruction encapsulation)	Guest: 5-Fluorouracil
	CAF@MIL-100_REC		Guest: Caffeine
	ASP@MIL-100_REC		Guest: Aspirin

[a] x: immersion time (e.g. 1, 2, 3…15 days)

2. Materials characterization

2.1. Inelastic neutron scattering

Inelastic neutron scattering (INS) measurements were performed using the TOSCA[1] spectrometer at the ISIS Pulsed Neutron and Muon Source, Rutherford Appleton Laboratory (Chilton, UK). The high-resolution ($\Delta E/E$~1.25%) and broadband (0-4000 cm^{-1}) spectra of each sample (~1 g) were acquired at ~10 K.

TOSCA is an indirect geometry time-of-flight spectrometer where a pulsed, polychromatic beam of neutrons collides with the sample at a distance of ~17 m from the source. The neutrons scattered from the sample were Bragg reflected by a pyrolytic graphite analyzer, while higher-order reflections beyond (002) were blocked by a cooled (T < 30 K) Beryllium filter in order to define the final energy. Neutrons with final energy of ~32 cm^{-1} were passed towards the detector array composed by thirteen ^3He tubes with effective length of 250 mm. Five banks were located in forward direction (scattering angle ~45°) and five in backwards direction (~135°). The use of a low final energy translated into a direct relationship between energy transfer (E_T, cm^{-1}) and momentum transfer (Q, $Å^{-1}$) such that $E_T \approx 16Q^2$. Energy transfer and spectral intensity, *i.e.* $S(Q, \omega)$, were then obtained using the Mantid software.[2] Each sample was wrapped in 4 cm × 4.6 cm aluminium sachet and placed into a 2.0 mm spaced flat aluminium cell, which was sealed with indium wire. Sample preparation and cell loading into the cell took place in a glovebox to avoid moisture uptake by the sample. To reduce the effect of the Debye-Waller factor on the experimental spectral intensity and allow comparison with the theoretical spectra, the sample cell was cooled to ~10 K by a closed cycle refrigerator (CCR). The INS spectra were collected under vacuum over a duration of 4-6 hours.

The neutron guide upgrade of the TOSCA spectrometer, completed in 2017, has increased the neutron flux at the sample position by as much as 82 times. This upgrade improves the performance through faster measurements and by reducing the required sample mass.[3]

2.2. Powder X-ray diffraction

The powder samples were analyzed by powder X-ray diffraction (PXRD) using the Rigaku MiniFlex diffractometer with a Cu K_α source (1.541 Å). Diffraction data was collected from 3° to 13°, using a 0.02° step size and 0.1° min^{-1} step speed. The patterns were then normalized with respect to the most intense peak in the pattern [0-1] used for the relative intensity of selected peaks. The raw PXRD data, however, were used for the calculation of FWHM peak broadening/sharpening.

2.3. Thermogravimetric analysis

Thermogravimetric analysis (TGA) was performed using TGA-Q50 (TA instruments). Approximately 4 mg of each sample was placed in a platinum pan (maximum volume 50 µL) and heated from 50 °C to 700 °C with a heating rate of 10 °C min^{-1}. The measurements for MIL-100 (Fe) samples were performed under a dry nitrogen flow of 40 mL min^{-1}. The measurements for drug@MIL-100 (Fe) samples were conducted under an air flow of 40 mL min^{-1} to guarantee complete decomposition of the guest molecules and accurate guest loading determination.

2.4. Attenuated total reflectance Fourier transform infrared spectroscopy

Attenuated total reflectance Fourier transform infrared spectroscopy (ATR-FTIR) spectra were acquired at room temperature with a Nicolet iS10 FTIR spectrometer with an ATR sample holder. The spectra were collected in the range of 650-4000 cm^{-1} with a resolution of 0.5 cm^{-1} and normalized in respect to the most intense vibrational peak to facilitate comparison across the different samples under study.

2.5. Scanning electron microscopy and atomic force microscopy

Analyses of the morphology and particle size determination were carried out by scanning electron microscopy (SEM) and atomic force microscopy (AFM). SEM images were obtained using Carl Zeiss EVO LS15 at 15 keV under high vacuum. Atomic force microscopy (AFM) was performed using the Veeco Dimension 3100 AFM equipped with an in-line optical zoom microscope with colour CCD camera for precise placement of probe onto the sample. The microscope was operated under the tapping mode, equipped with a Tap300G silicon probe with resonance frequency of 30 kHz, spring constant of 40 Nm^{-1}, and tip radius < 10 nm.

2.6. Specific surface area measurements

The Brunauer-Emmett-Teller (BET) specific surface areas of samples were determined from nitrogen adsorption-desorption isotherms at 77 K, measured with Quantachrome Nova 1200. The isotherms were obtained using a Ø9 mm sample cell containing 60-100 mg of samples under study. The degassing temperature was 150 °C during sample activation under vacuum.

2.7. Density functional theory calculations

Density functional theory (DFT) calculations to determine the theoretical vibrational spectrum of H_3BTC was performed using the Gaussian software.[4] The vibrational calculation was carried out at the B3LYP level of theory and 6-31G basis set. We used the DFT output file of this study to generate the INS spectrum using the Mantid software[2] through the AbINS extension.[5] During the spectrum generation a total cross section was considered with a quantum order events number of 1.

2.8. Calculation of PXRD peaks height and full width at half maximum of ATR-FTIR peaks

The Integrate Gadget in OriginPro software was used to perform the numerical integration on the PXRD patterns and determine the full width at half maximum (FWHM) of two of the most intense diffraction peaks in the MIL-100 (Fe) samples (i.e. $2\theta = 4°$ and 11°) that correspond to the (022) and (357) planes. The range of data was selected to include the peaks of the diffraction pattern of interest, using the (horizontal) diffraction angle axis as the baseline. The same approach was used for the obtaining the FWHM of ATR-FTIR vibrational bands. To facilitate the comparison between the effect of the reconstruction process, the ratio between the peak heights [(022):(357)] was taken and the FWHM values were normalized against the largest value presented within a set of samples.

2.9. Acidity measurements of immersion solutions

The pH values of the immersion solutions were determined using a Fisherbrand pH indicator paper stick that was compared against a pH scale and across all the samples in the study.

2.10. Proton acceptor/donor sites and electrostatic potential surface map determination

The proton acceptor/donor sites present in the guest drug molecules (*e.g.* 5-fluorouracil, caffeine, and aspirin) were determined using BIOVIA Discovery Studio. The electrostatic potential (ESP) surface maps of drug molecules were generated using GaussView. During the map generation, the electron density was calculated from a Total SCF density with isovalue of 0.000400 electrons per unit volume (au^3).

2.11. Fabrication of pellets

Pellets were prepared on a manual hydrostatic press (Specac) with a die diameter of 13 mm and under a constant axial force that varied tom 0.5 to 10 ton. Each pellet was produced using 175 mg of the MOF material.

3. Results and Discussion

3.1. Reconstruction of as-synthesized MIL-100 (Fe)

The effect of the reconstruction process has been monitored *via* analysis of the PXRD data. The evolution of the relative peak intensity [*i.e.* (022):(357) ratio] and of the change in FWHM at low diffraction angles (2θ = 4° and 11°) has been monitored as a function of the sample immersion time.

The Scherrer law allows one to determine the size of the crystalline domains *D*:[6]

$$D = \frac{K\lambda}{\Delta cos\theta}$$

where λ is the wavelength, Δ = FWHM, *K is* a constant, and θ is the diffraction angle of the corresponding diffraction peak.

As the samples might present different particle sizes (from 100s of micrometers to 10s of nanometers) and different packing configurations, the best representation to establish the cross comparison of such samples was chosen as the "crystallinity" where:

$$Crystallinity = \frac{D_{\text{initial}}}{D_{\text{x}}}$$

With *x* referring to the different immersion times. Then:

$$Crystallinity = \frac{\frac{K\lambda}{\Delta_{\text{initial}} cos\theta}}{\frac{K\lambda}{\Delta_{\text{x}} cos\theta}} = \frac{\Delta_{\text{x}}}{\Delta_{\text{initial}}}$$

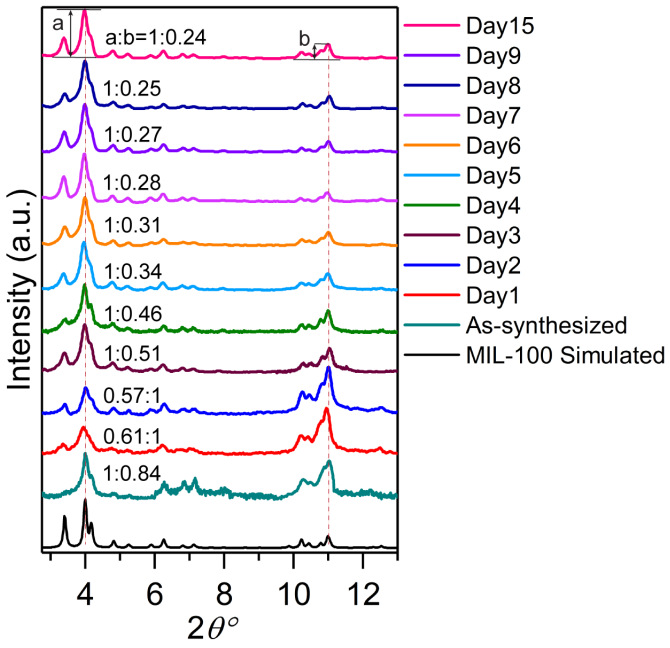

Figure S1. Normalized PXRD patterns of MIL-100 (Fe) after different immersion times. Each pattern presents the ratios of the changing relative intensity of the a:b = (022):(357) planes, demonstrating the progressive increase in the relative intensity of the (022) plane.

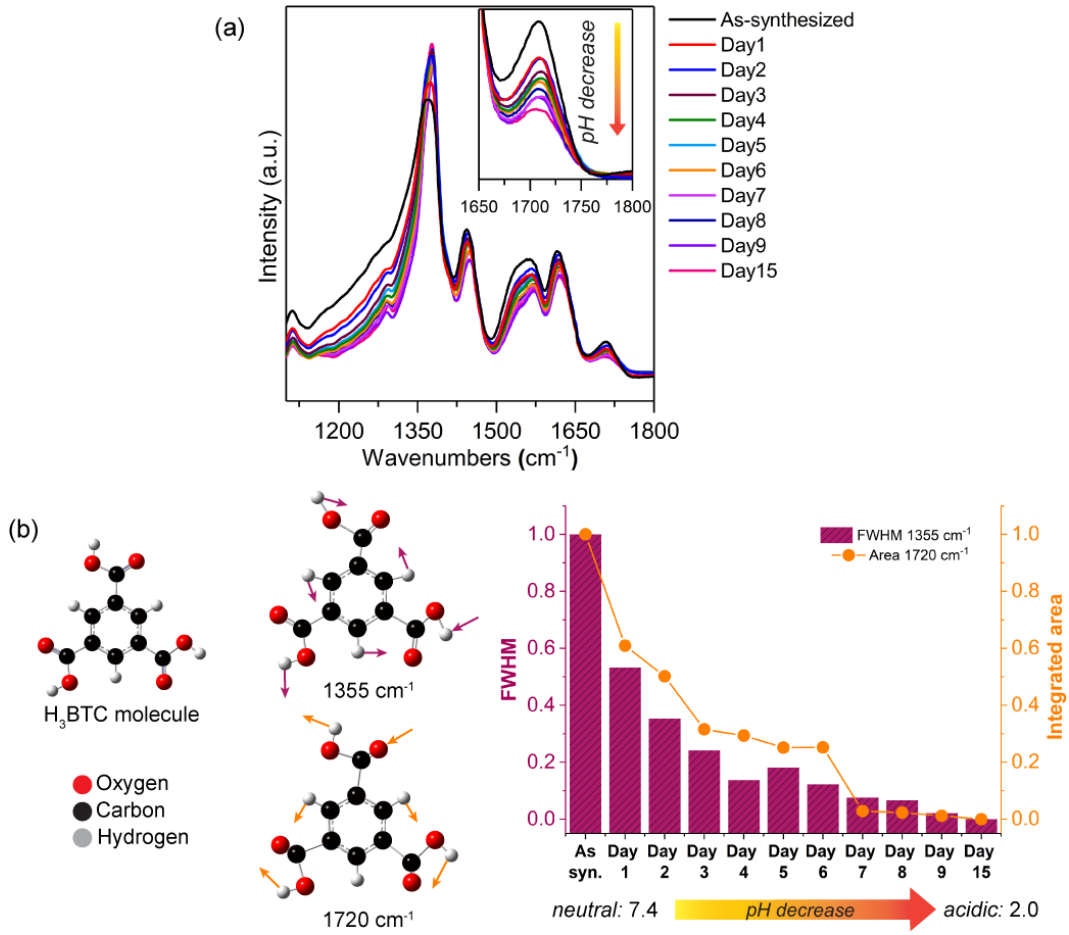

Figure S2. (a) Sharpening of the carboxylate vibrational band at ~1355 cm^{-1} and the decrease in intensity of the C=O stretching of H_3BTC at ~1720 cm^{-1}, expressed numerically by (b) FWHM values and integrated area, respectively. Colour code: O in red, C in black, and H in grey.

3.2. BET surface area of MIL-100 (Fe) samples

To acquire deeper insights into the reconstruction process, four samples collected at different immersion times (*i.e.* 2, 4, 7 and 12 days) were selected for nitrogen adsorption and desorption measurements. Evaluation of the nitrogen isotherms shapes (Figure 2b) coupled with the Brunauer–Emmett–Teller (BET) surface area determination (Table S2) allowed us to classify the samples porosity and assess its evolution during the reconstruction process. The change in the pore structure was accompanied by the increase in the BET surface area.

Table S2. Comparison of the BET surface area of MIL-100 samples produced *via* various methods

	Sample	Synthesis method	BET surface area ($m^2.g^{-1}$)	Reference
	MIL-100 as-synthesized	Mechanochemistry (manual grinding)	157	This work
Reconstruction process	MIL-100 Day 2	Mechanochemistry followed by water immersion	667	
	MIL-100 Day 4		720	
	MIL-100 Day 7		735	
	MIL-100 Day 12		997	
	5-FU@MIL-100_REC	REC: encapsulation during reconstruction	435	
	CAF@MIL-100_REC		223	
	ASP@MIL-100_REC		225	
Time degraded sample	MIL-100 aged (1.5 years of shelf life)	Mechanochemistry (manual grinding)	521	
	MIL-100 aged reconstructed	Water immersion	767	
Mechanically amorphized sample	MIL-100 crushed pellet (10 ton)	Mechanochemistry (manual grinding)	14	
	MIL-100 crushed pellet reconstructed	Water immersion	276	
MIL-100 (Fe)		Mechanochemistry (high pressure and temperature)	1940	Han *et al.*[7]
		Mechanochemistry (Liquid assisted grinding - ball mill)	1033	Pilloni *et al.*[8]
		Mechanochemical (kitchen grinder)	255	Samal *et al.*[9]
		Solvothermal (high temperature)	1836	Zhang *et al.*[10]
		Solvothermal (high pressure and temperature)	1750	Chen *et al.*[11]
		Solvothermal (high pressure and temperature)	1223.32	Zhang *et al.*[12]
		Solid state synthesis (high pressure and temperature)	110.49	Chaturvedi *et al.*[13]

We have compared the synthesis parameters (*i.e.* total synthesis time and required temperature) of approaches conventionally used for the fabrication of MIL-100 (Fe), some newly employed mechanochemical methods and the mechanochemical-reconstruction method herein applied based on the resulting BET surface area achieved (Figure S3).

Our as-synthesized MIL-100 (Fe) material has shown higher surface area when compared to the material obtained *via* the solid-state approach (Chaturvedi *et al.)*, conducted under high pressure conditions. The surface area of our material is significantly improved after the reconstruction process (*i.e.* MIL-100 Day 12) and is comparable to those obtained by solvothermal and ball milling approaches (Pilloni *et at.)*, which require the use of more extreme conditions (high temperature and pressure) and the use of corrosive toxic agents.

.

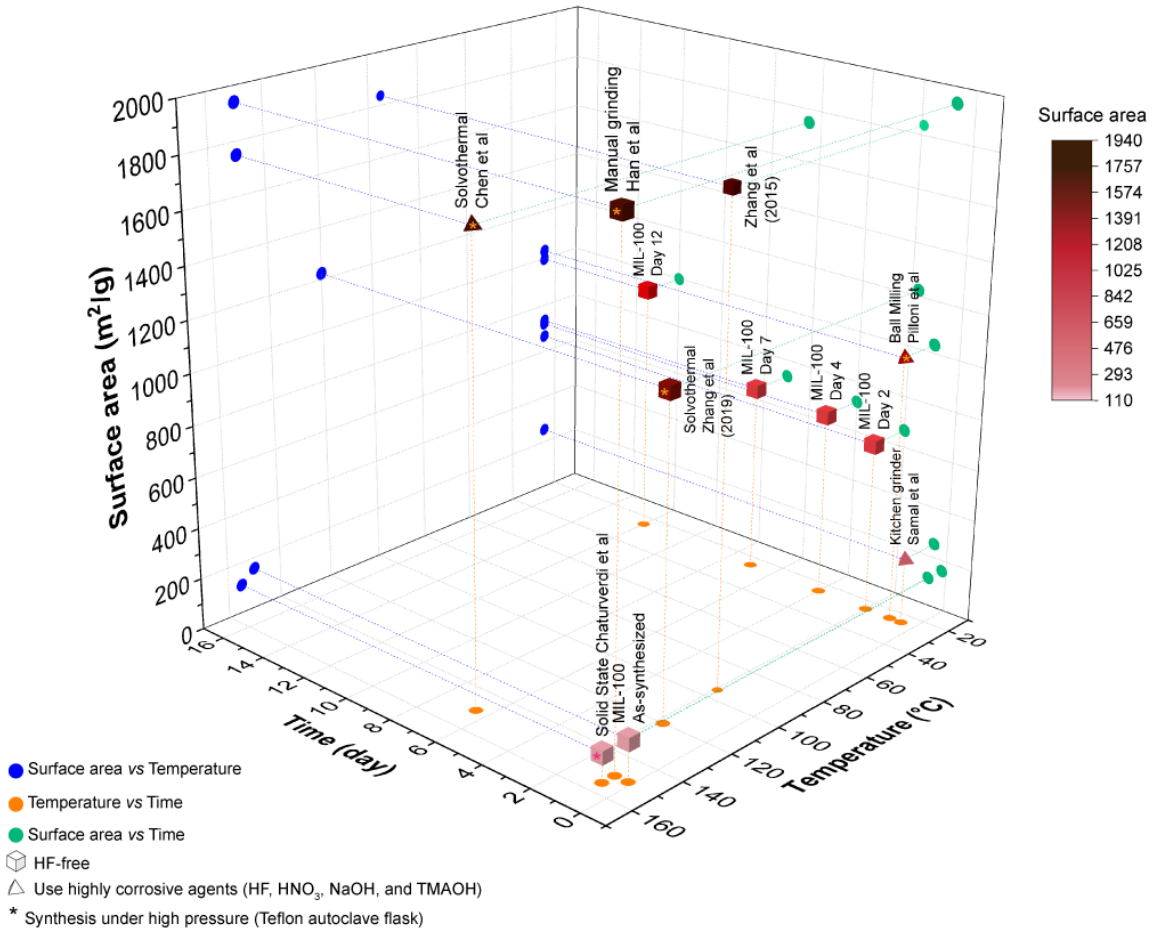

Figure S3. Comparison of BET surface area, synthesis temperature and total synthesis time of MIL-100 (Fe) samples prepared in this work *via* the reconstruction technique and the reported BET surface area of MIL-100 (Fe) fabricated *via* various synthetic methods.

3.3. Morphological characterization of MIL-100 (Fe) sample

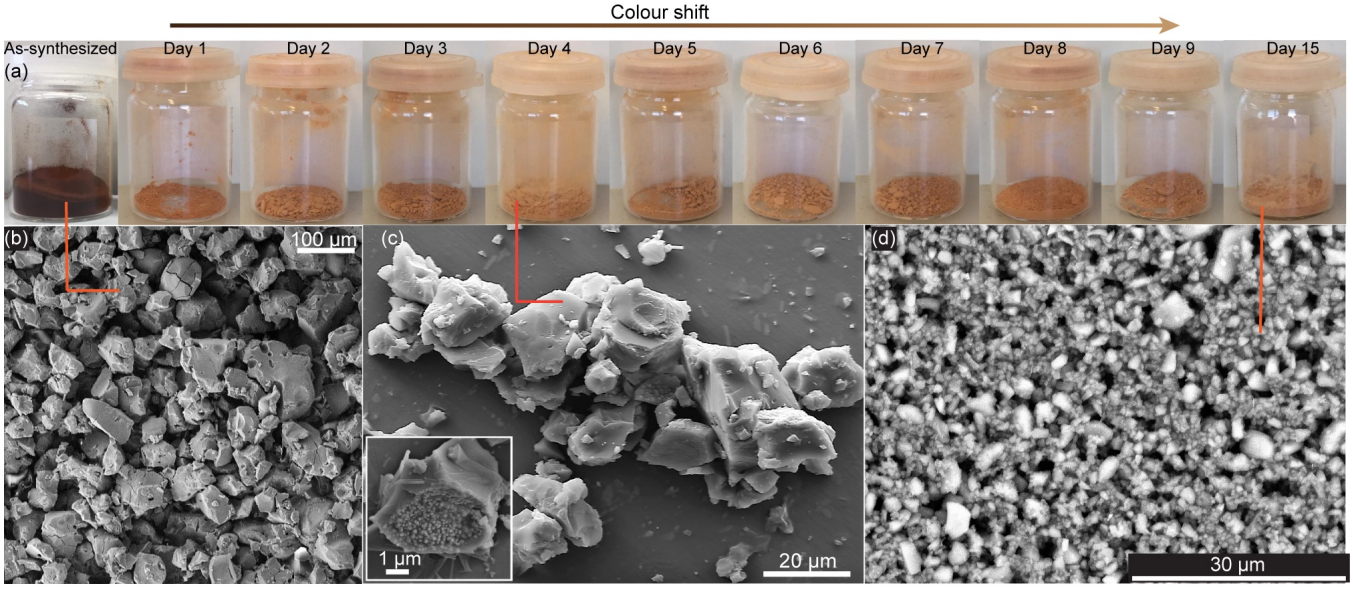

Figure S4. SEM images of MIL-100 (Fe) samples. (a) Photographic representation of MIL-100 (Fe) samples collected at different immersion time intervals. The change in the sample color can be associated to changes in the aggregation of particles as observed in (b), (c) and (d), respectively.

MIL-100 (Fe) Day 12 sample was used for the fabrication of pellets under different uniaxial forces. All pellets were produced from the same batch of material, and presented good mechanical strength, being able to be manipulated by hand. As the pelletizing force increased, a colour shift was observed with the darkening of the pellets as a result of the denser packing of MIL-100 (Fe) nanoparticles. This effect reproduces the optical changes shown in Figure S4.

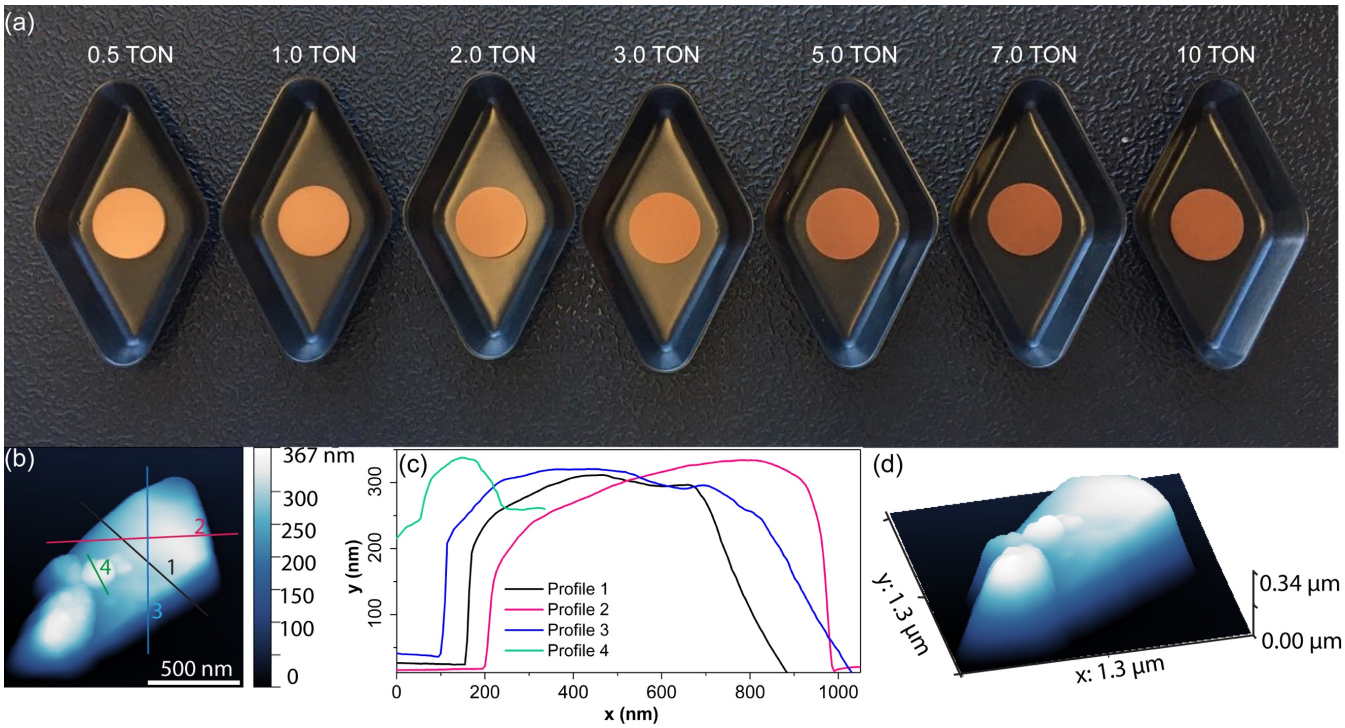

Figure S5. (a) Pellets of MIL-100 (Fe) samples produced by the application of various uniaxial forces. The packing of the MIL-100 particles demonstrates that shifts in the colour of the pellets, going from light to dark brown, are observed as the particles become more densely packed (i.e. subjected to 0.5 to 10 ton). (b) AFM image of MIL-100 (Fe) Day 12 crystals used to produce the pellets displayed in (a). (c) Height profile of crystals revealing the size and shape of MIL-100 (Fe) Day 12 crystals, with a rectangular-like shape of hundreds of nanometers. (d) 3D view of crystal displayed in (b).

3.4. Reconstruction of aged-MIL-100 (Fe)

Using the reconstruction strategy, we were able to recover the crystallinity of MIL-100 (Fe) samples with a shelf age of 1.5 years. Throughout this time, the samples have been stored in a standard sealed vial. As observed in Figure S6a, the aged-MIL-100 (Fe) showed signs of decomposition/collapse due to the change in the relative intensity of the planes (022):(357), going from 1:025 to 1:0.99 for the as-synthesized and aged samples, respectively. The (022) plane seemed to suffer the most from the aging of the sample, with large reduction of intensity. As it can be noted from Figure S6c, the (022) peak has shown large broadening after the aging process.

Via the reconstruction process (Figure S6b) the crystallinity of the material was increasingly recovered with the increase of immersion time. Not only the relative intensity of the samples presented a massive change (from 1:0.99 to 1:0.26), but also the FWHM values of the (022) peak were fully restored.

Concomitantly, as shown in Figure S7, the broadening of the carboxylate vibration band at 1355 cm^{-1} in the aged sample and the sharpening of this same band after the reconstruction process indicates the increase in the structural symmetry of the sample. Moreover, the BET surface area presented a recovery of 96.7% against the initial value, demonstrating the reconstruction of the materials porosity.

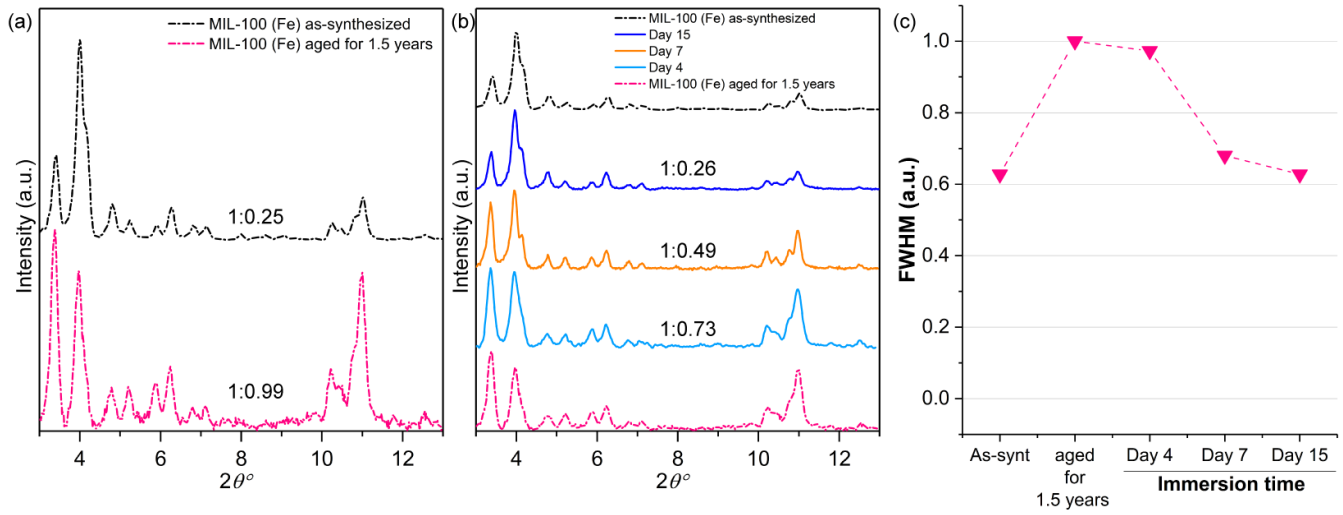

Figure S6. PXRD patterns of aged samples used in the reconstruction process. (a) PXRD pattern of fresh MIL-100 (Fe) (black trace) and the aged sample (pink trace). (b) PXRD patterns showing the recovery of crystallinity of the aged sample after immersion in DI water. (c) FWHM of the (022) plane.

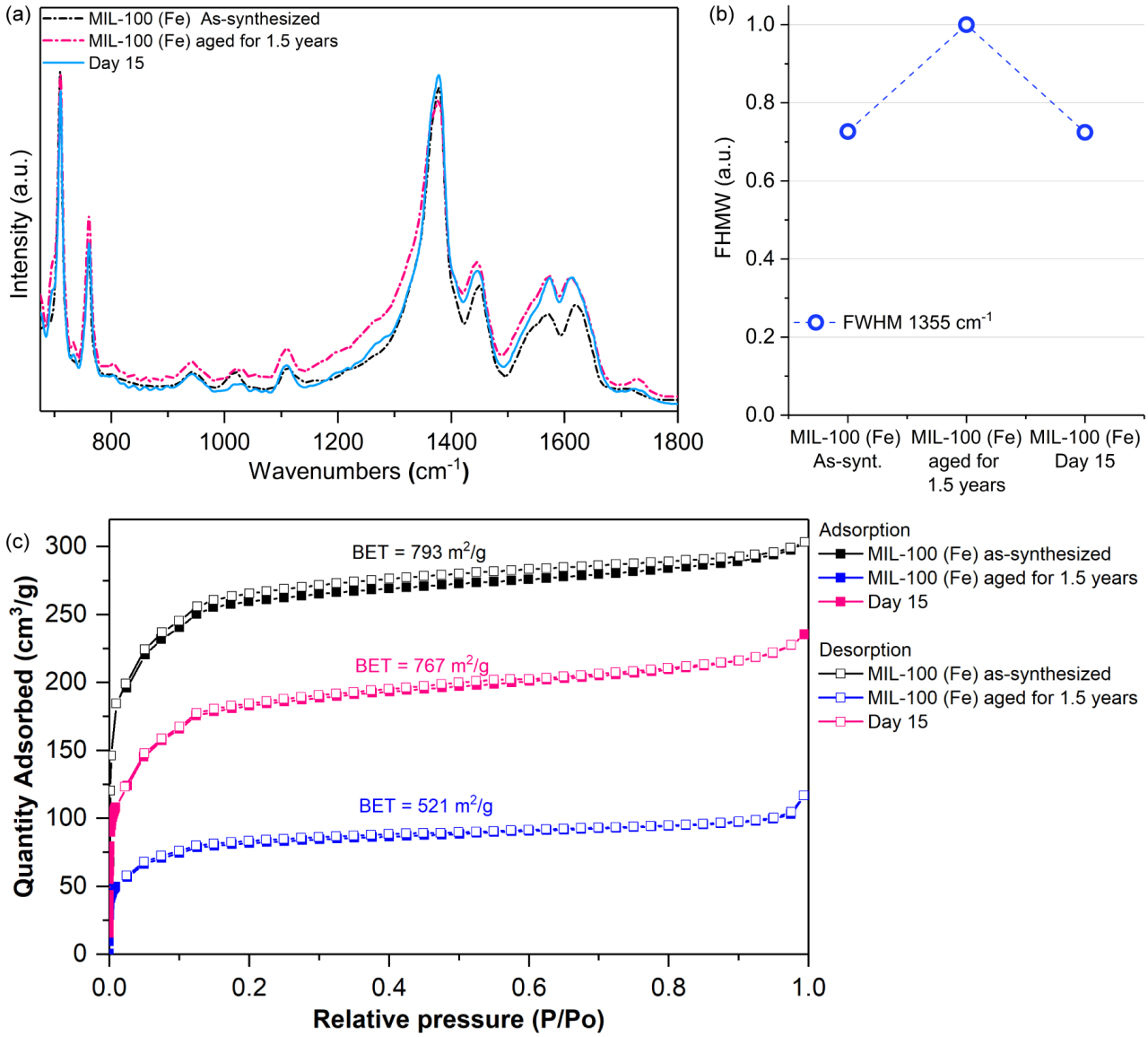

Figure S7. Analysis of vibrational data of the reconstructed aged sample. (a) ATR-FTIR spectra of aged samples under reconstruction. (b) FWHM values of vibration band at ~1355 cm^{-1} highlighting the sharpening of carboxylate vibration after the reconstruction process. (c) Nitrogen adsorption and desorption isotherms of time degraded MIL-100 (Fe) samples under reconstruction. Samples were activated at 150 °C under high vacuum for 12 hours prior to the N_2 adsorption measurements at 77 K. The BET surface area presented a recovery of 96.7% versus the initial value.

The reconstruction process has also been successfully used for the recovery of crystallinity of mechanically amorphized samples. As demonstrated in Figure S8, the diffraction peaks at 4° and 11° vanish after the pelletizing process. Concomitantly, as it can be seen from Figure S9c, the material is almost non-porous with a much reduced surface area of 14.22 m^2/g.

After relaxation of the structure (*i.e.* crushing the pellet back to powder) some of the most intense diffraction peaks reappeared. However, the relative intensity of (022):(357) peaks is very distinct from the original powder used for the production of the pellets. The above ratio was almost completely restored after 7 days of immersion in DI water.

Similar to what was observed during the reconstruction of the aged samples, Figure S9 shows the broadening of the carboxylate vibration band at 1355 cm^{-1} after pelletizing and the sharpening of the same band after the reconstruction process, indicating the increase in the structural symmetry of the sample.

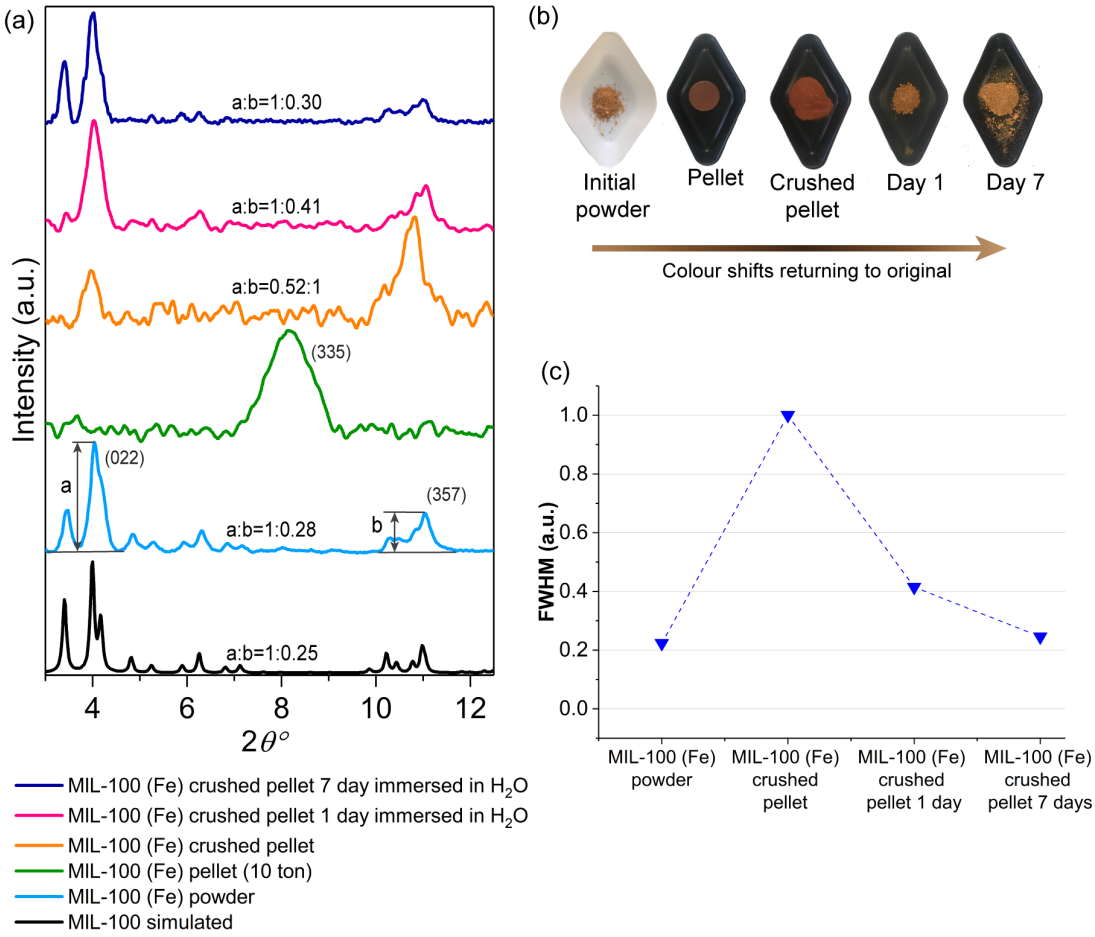

Figure S8. Reconstruction of mechanically amorphized samples. (a) PXRD patterns showing the progressive change in the relative intensity of the diffraction peaks. (b) Colour shift presented by the samples during the reconstruction process in which the original colour is restored demonstrating changes in the microstructure/optical properties of the material. (c) FWHM used to assess the sharpening of the (022) peak. As it can be observed, after the pelletizing, the diffraction peak corresponding to the (022) plane becomes very broad. However, the FWHM values are virtually restored to the pristine material values after the reconstruction process.

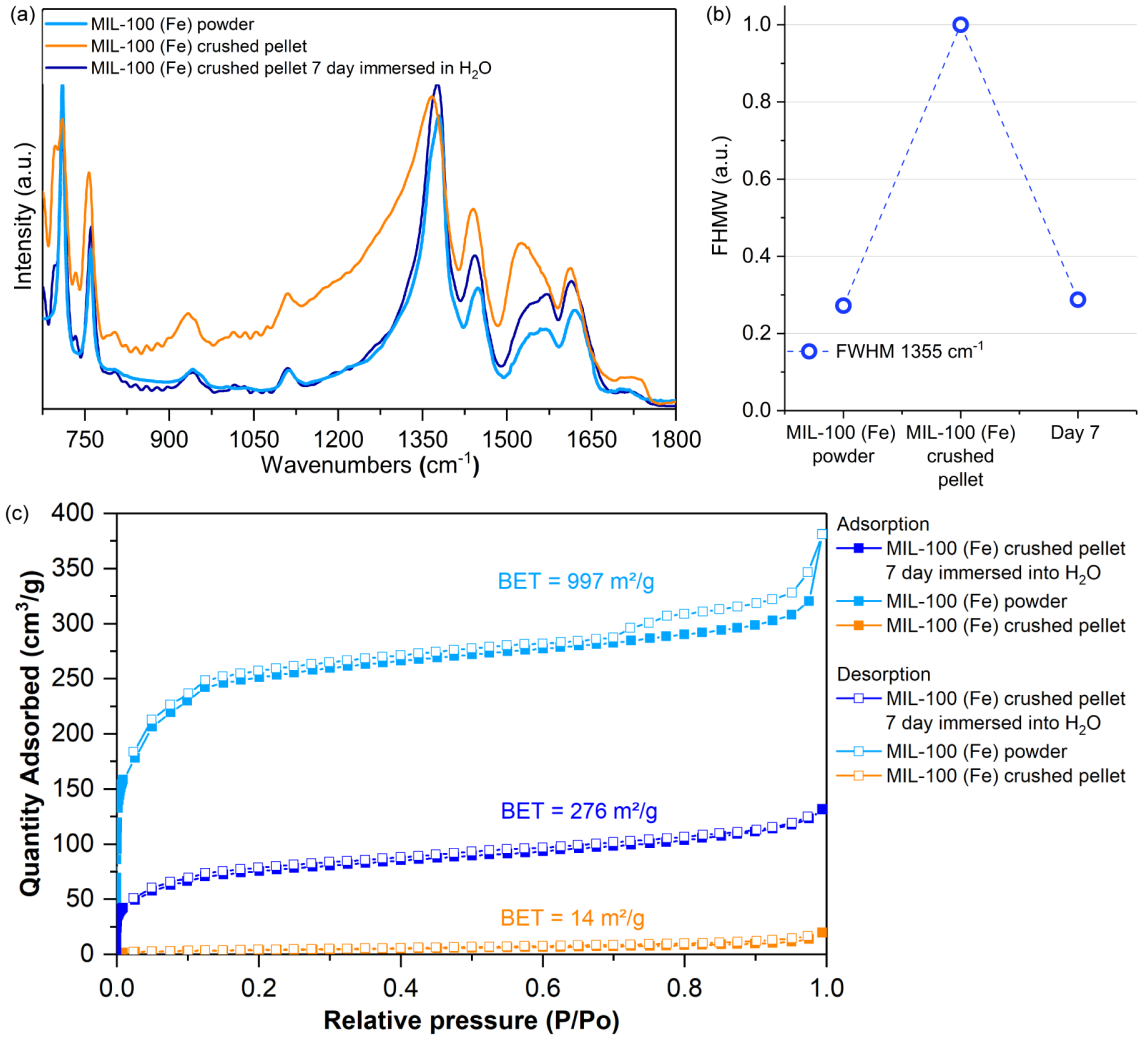

Figure S9. Analysis of vibrational data of reconstruction of pellet sample. (a) ATR-FTIR spectra of pelletized samples under reconstruction. (b) FWHM values of vibrational band at ~1355 cm^{-1} highlighting the sharpening of carboxylate vibration after the reconstruction process. (c) Nitrogen adsorption and desorption isotherms of mechanically amorphized MIL-100 (Fe) samples under reconstruction. Samples were activated at 150 °C under high vacuum for 12 hours prior to the N_2 adsorption measurements at 77 K. The BET surface area presented a recovery of only 27.7% compared to its initial value.

3.5. Examination of organic ligand H_3BTC INS spectrum

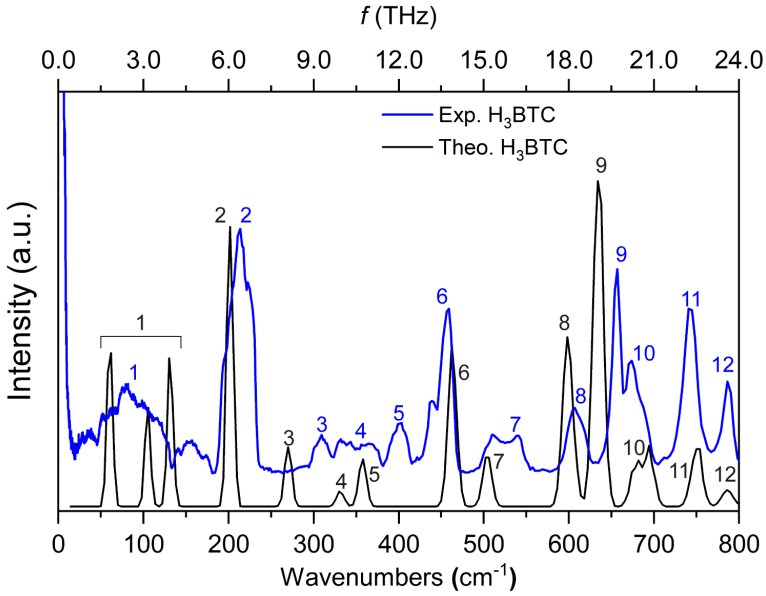

Figure S10. Comparison between experimental (blue) and theoretical (black) DFT spectra of H_3BTC. Numbers were used to facilitate the identification of the vibrational modes. Good agreement between both spectra is observed in the low energy region.

Table S3. Description of vibrational modes of H_3BTC in the range of 0-800 cm^{-1} [14]

Mode no.	Theo. (cm^{-1})	Exp. (cm^{-1})	Description
1	20-133	21-183	γCOOH, γCO, and γ ring including trampoline-like motion
2	218	202	γCO
3	272	273	δCO
4	332	334	
5	361	358	γ ring and γOH
6	470	464	δCC and δOH
7	505	506	δCO and δCH
8	603	600	γ ring and γOH
9	635	636	δOH and δCH
10	674	685	
11	714	750	δCO and δCC
12	780	786	

δ, in-plane bending, γ, out-of-plane bending.

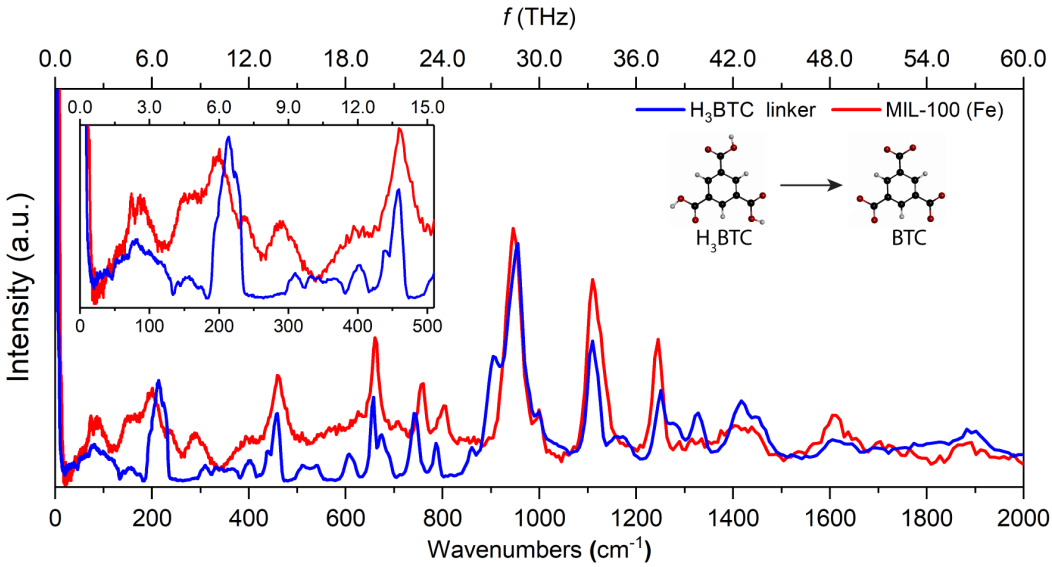

Figure S11. INS spectra of pristine MIL-100 (Fe) sample (red) and organic linker H_3BTC (blue). Good agreement is observed between framework modes and organic linker modes, helping us to pinpoint in the MOF spectrum the vibrational modes related to the organic linker. Note that the H_3BTC spectrum was scaled down by a factor of 0.3 to facilitate comparison with the MOF spectrum. Colour code: O in red, C in black, and H in grey.

3.6. Thermal stability of MIL-100 (Fe) reconstructed samples

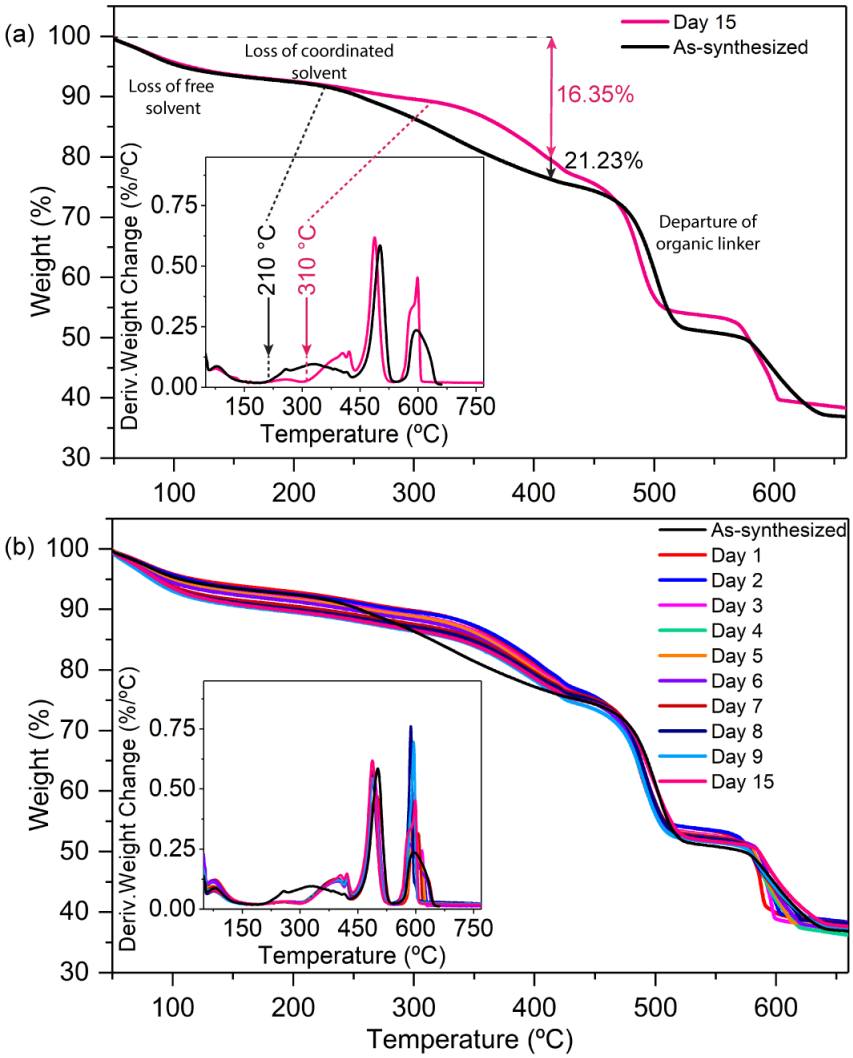

Figure S12. TGA of MIL-100 (Fe) samples with insets showing the differential material decomposition behaviour as a function of temperature. (a) Contrast between the as-synthesized MIL-100 (Fe) and reconstructed MIL-100 (Fe) after 15 days of immersion time. An increase in the thermal stability of the material is observed (~100 °C difference in the initial decompostion temperature of the material). (b) Contrast between TGA of as-synthesized sample and samples subjected to different immersion times.

Table S4 displays details of the decomposition process of MIL-100 (Fe) sample acquired from the TGA plots (Figure S12). A large increase in the initial decomposition temperature of the crystalline MIL-100 (Fe) in comparison to the as-synthesized material can be observed. A decrease (~20%) in the rate of the composition between 210-450 °C was also noticed. Meanwhile, the maximum rate of decomposition, the temperature in which half of the material has decomposed and the final residue have remained virtually unchanged.

Table S4. Analysis of decomposition of MIL-100 (Fe) samples.

	Initial decomposition temperature	Rate of decomposition (210 °C - 450 °C)	Maximum rate of decomposition	Temperature of half decomposition	Final residue (at 660 °C)
As-synthesized	210 °C	-0.076 %/°C	-0.275 %/°C	574 °C	37%
MIL-100 (Fe) Day 15	310 °C	-0.061 %/°C	-0.289 %/°C	578 °C	38%

3.7. SEM images of drug@MIL-100 systems

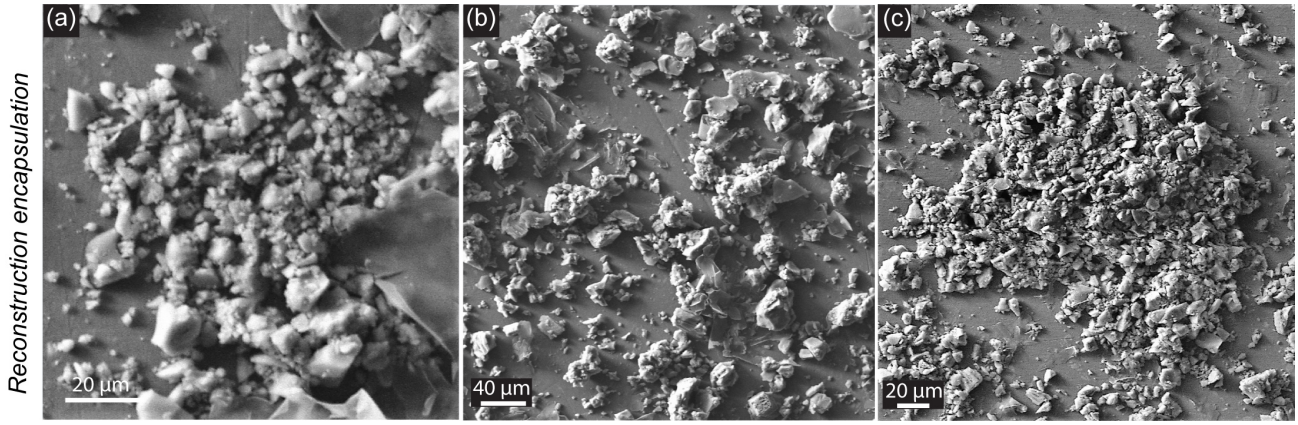

Figure S13. SEM images of guest@MIL-100 systems. (a) 5-FU@MIL-100_REC, (b) CAF@MIL-100_REC, and (c) ASP@MIL-100_REC.

3.8. Diffraction data analysis of drug@MIL-100 systems

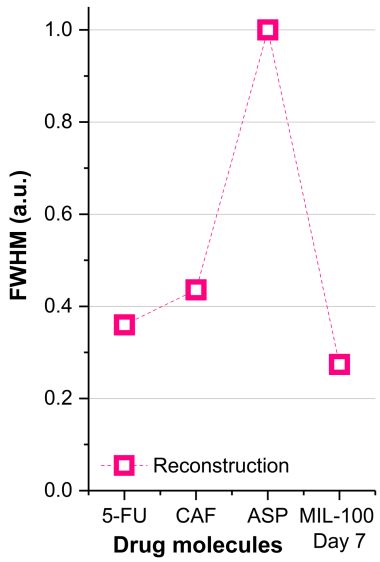

Figure S14. FWHM used to assess the sharpening of the (022) peak in the drug@MIL-100 systems, contrasting the effect of the different guest drug molecules being used. The plots evidence the strong effect on the material crystallinity that aspirin has in comparison to the other drug molecules when the reconstruction strategy is applied for the encapsulation of the guest molecules. To facilitate the comparison, the values have been normalized in relation to the highest FWHM value among this set of samples.

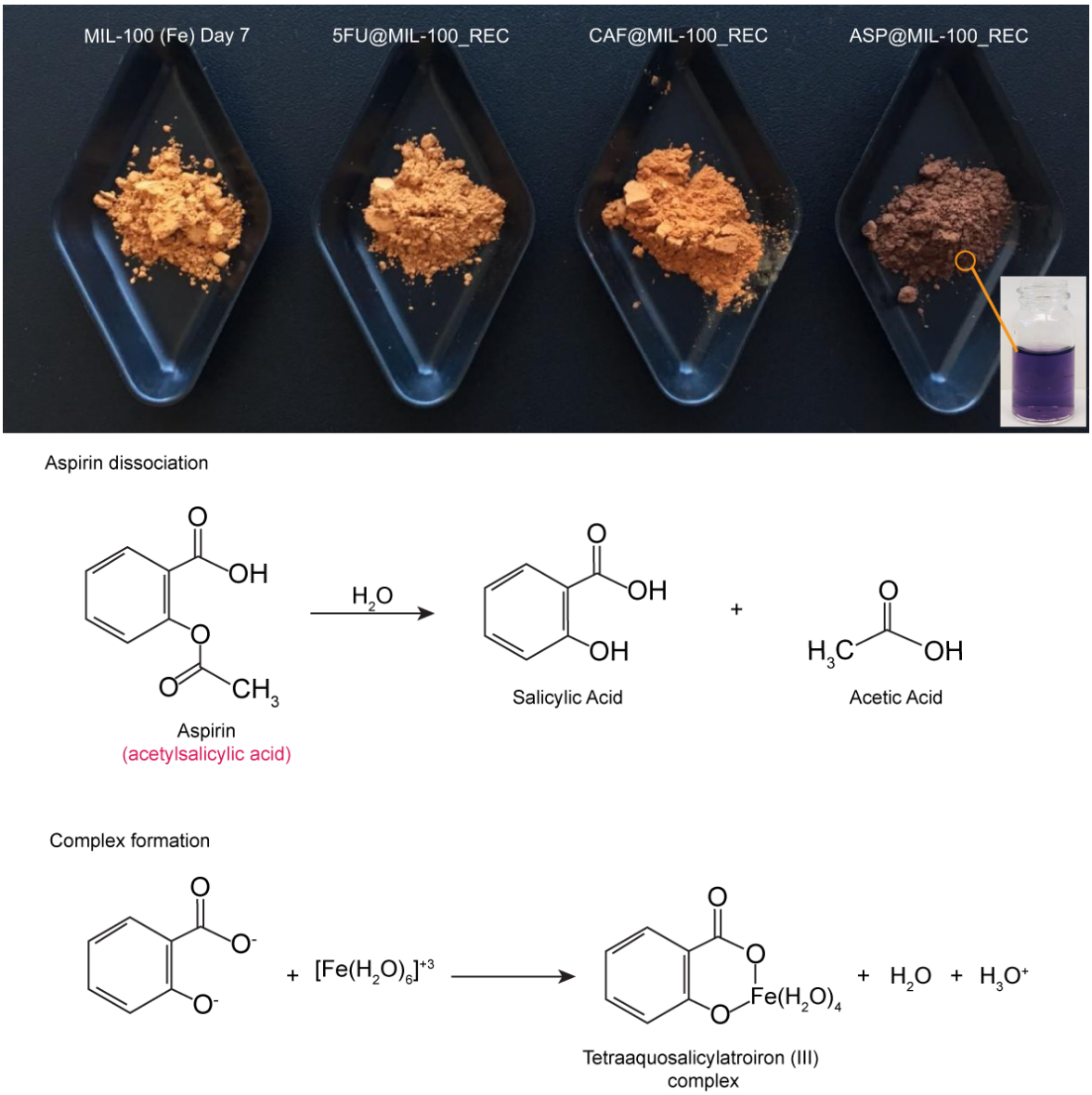

Figure S15. Photograph showing the various MIL-100 (Fe) samples after the encapsulation-reconstruction process, showing a distinct colour difference between 5-FU@MIL-100_REC and CAF@MIL-100_REC to ASP@MIL-100_REC. This is due to the formation of a violet aspirin-iron complex known as tetraaquosalicylatroiron (III) complex (inset). When in contact with moisture, aspirin dissociates into acetic and salicylic acid. The latter then can react with acidified iron (III) ions to form the violet complex.

3.9. INS spectra of MIL-100 (Fe) and guest@MIL-100 systems

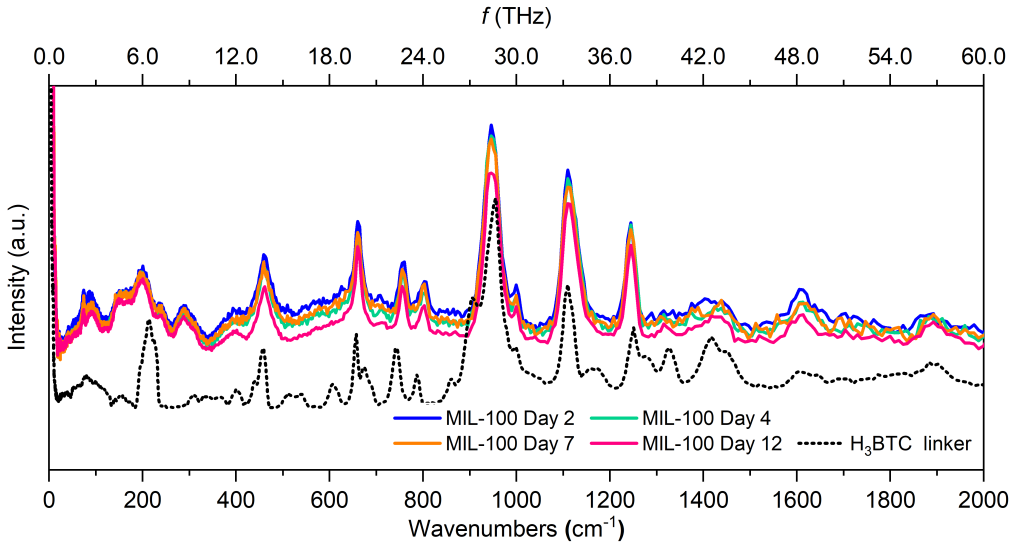

Figure S16. INS spectra of MIL-100 (Fe) samples collected after different immersion times. In black is the spectrum of H_3BTC linker which was scaled down by a factor of 0.2 to facilitate the comparison with MOF spectra.

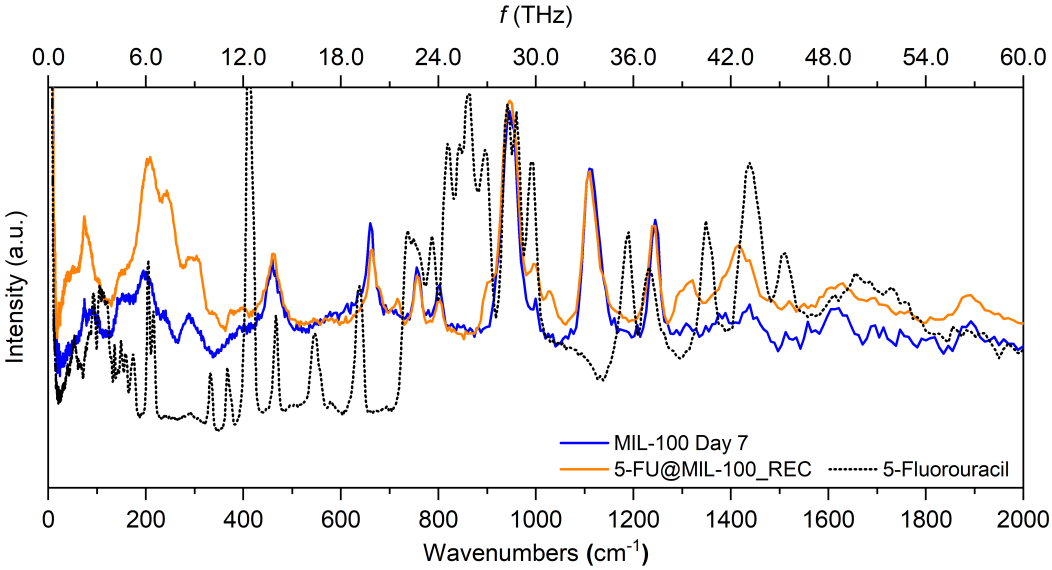

Figure S17. INS spectra of 5-FU@MIL-100 yielded by the reconstruction and *in situ* encapsulation techniques. Spectrum of 5-FU presented in black was scaled down by a factor of 0.4 to facilitate the comparison with the guest@MIL-100 systems.

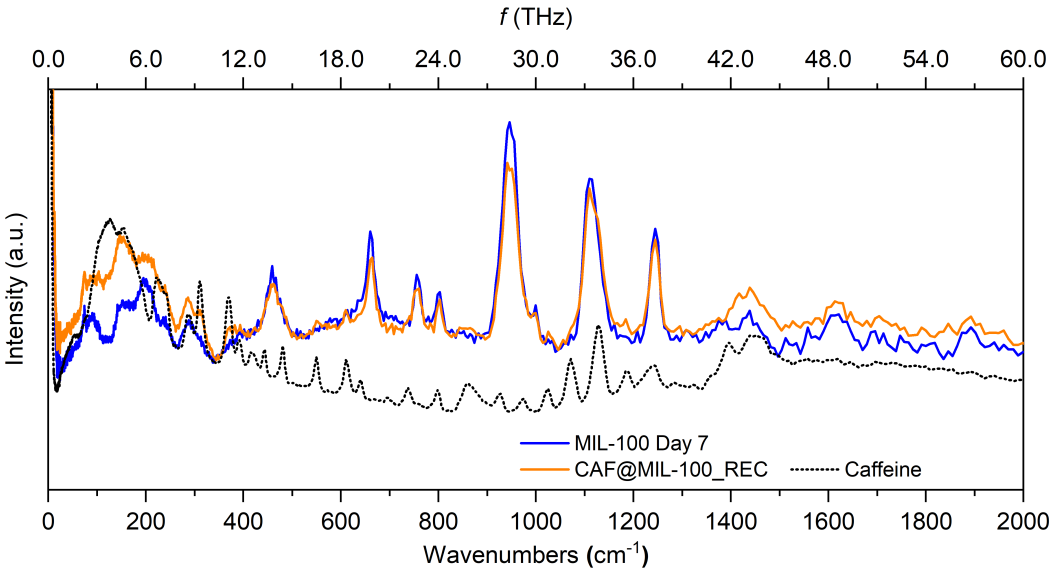

Figure S18. INS spectra of CAF@MIL-100 yielded by the reconstruction and *in situ* encapsulation techniques. Spectrum of caffeine presented in black was scaled down by a factor of 0.2 to facilitate the comparison with the guest@MIL-100 systems.

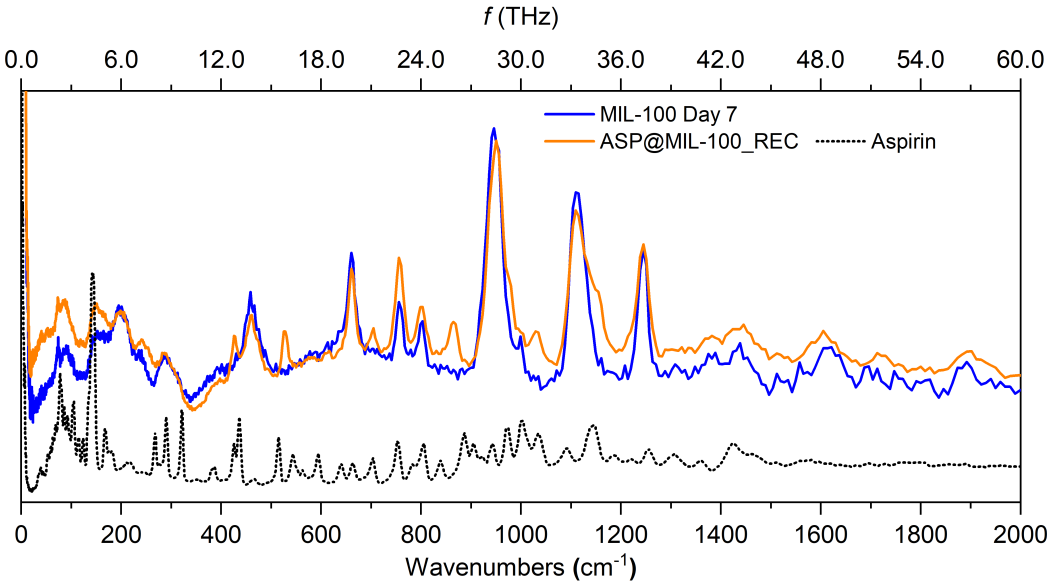

Figure S19. INS spectra of ASP@MIL-100 yielded by the reconstruction and *in situ* encapsulation techniques. Spectrum of aspirin presented in black was scaled down by a factor of 0.1 to facilitate the comparison with the guest@MIL-100 systems.

3.10. ATR-FTIR spectra of guest@MIL-100 systems

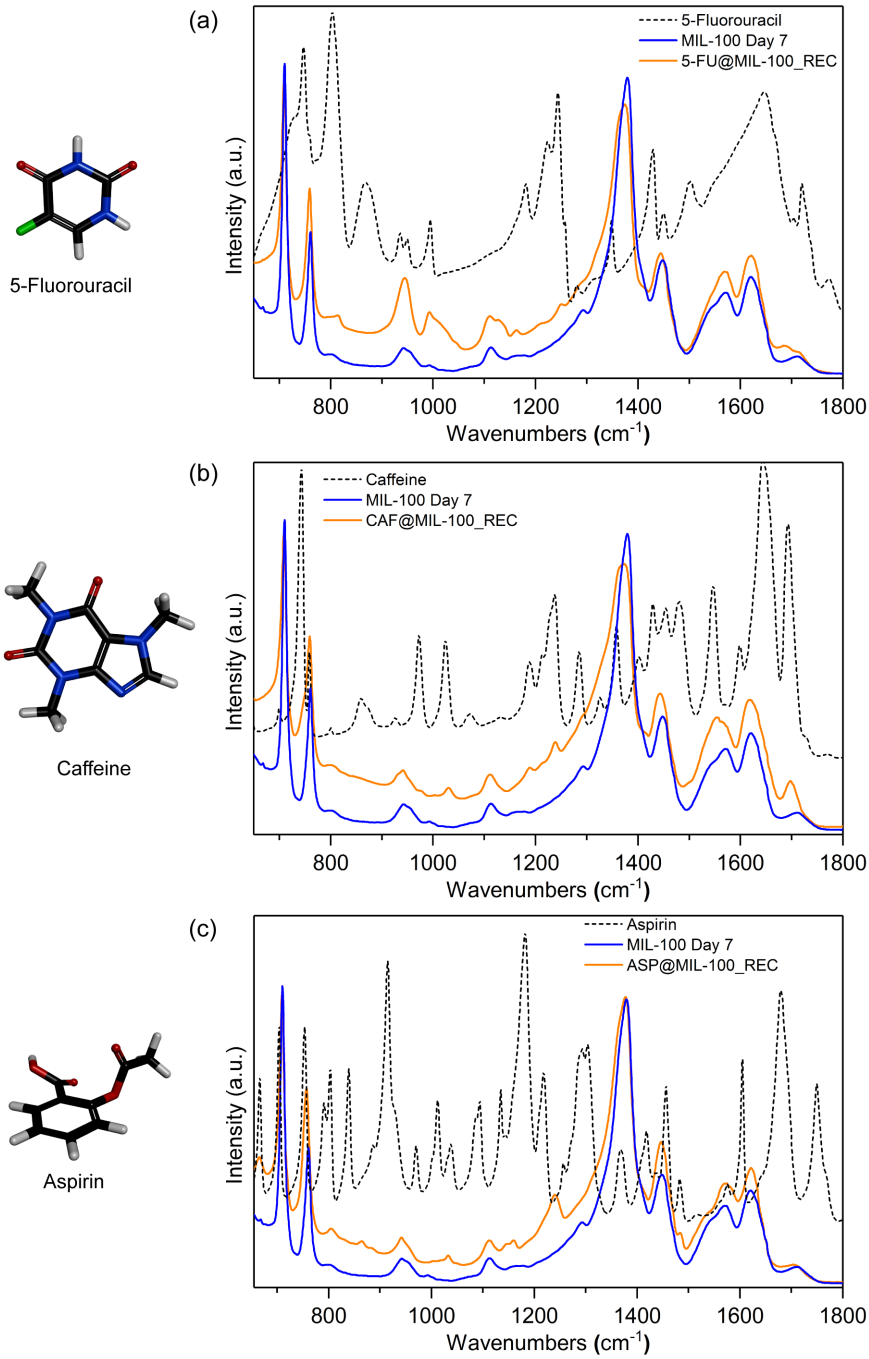

Figure S20. ATR-FTIR spectra of guest@host systems displaying (a) 5-FU@MIL-100_REC, (b) CAF@MIL-100_REC, and (c) ASP@MIL-100_REC. For comparison, the spectrum of MIL-100 (Fe) after 7 days of immersion time was also presented. Colour code: O in red, C in black, H in grey, N in navy blue, F in green.

3.11. Evaluation of guest encapsulation *via* thermogravimetric analysis and nitrogen adsorption/desorption

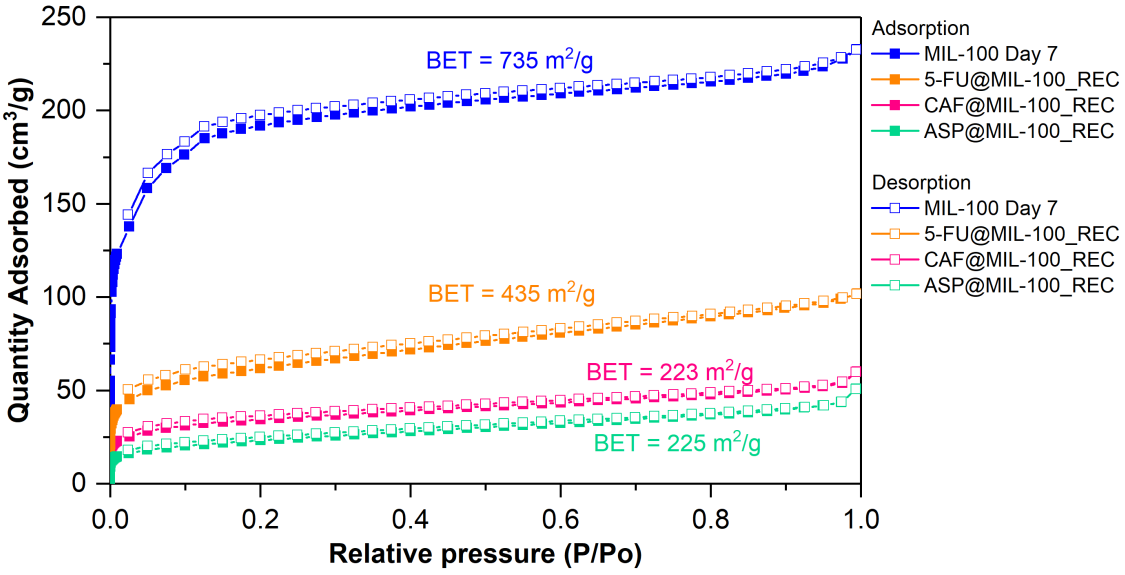

Figure S21. Nitrogen adsorption and desorption isotherms of 5-FU@MIL-100_REC, CAF@MIL-100_REC, and ASP@MIL-100_REC systems.

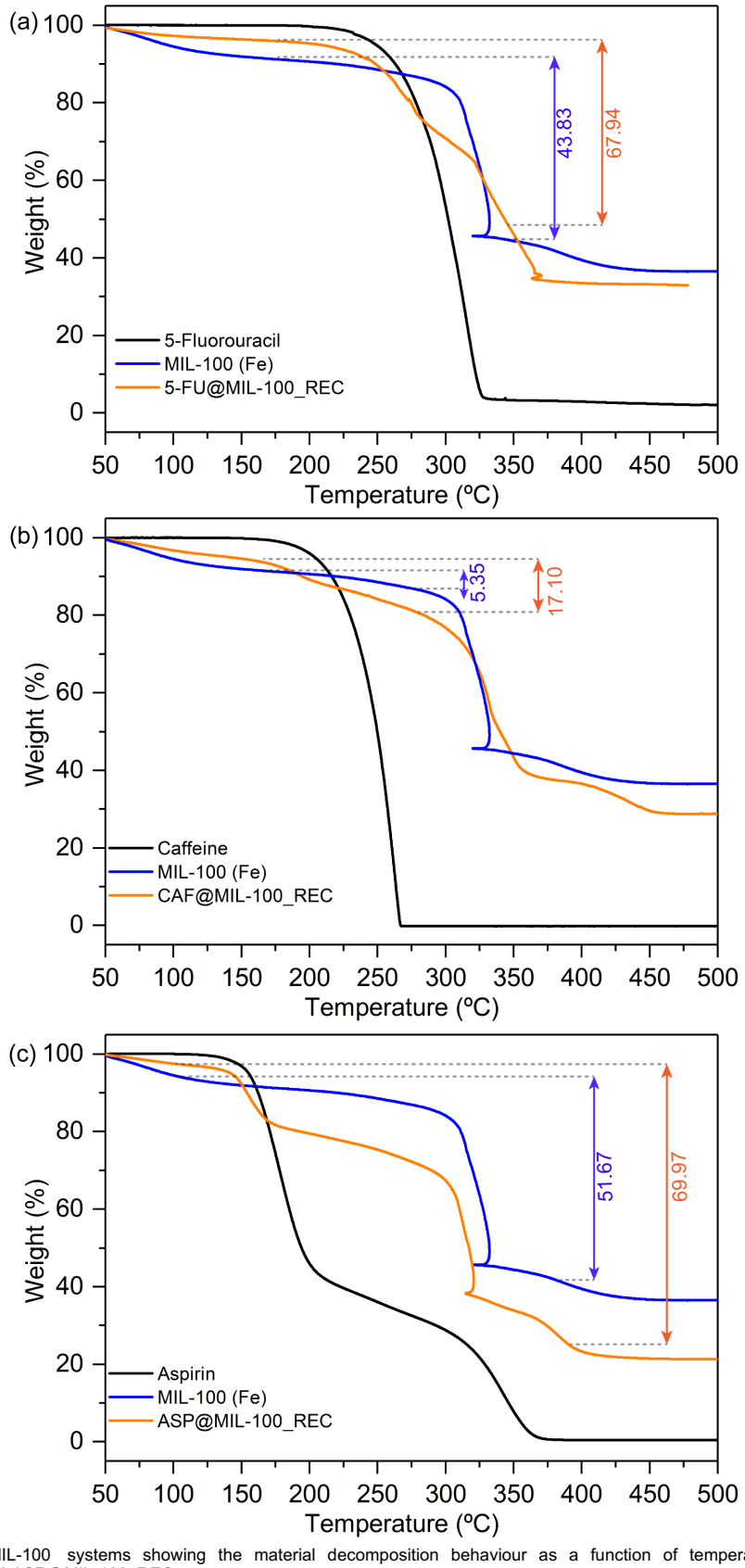

Figure S22. TGA of drug@MIL-100 systems showing the material decomposition behaviour as a function of temperature. (a) 5-FU@MIL-100_REC, (b) CAF@MIL-100_REC, and (c) ASP@MIL-100_REC.

Table S5. Comparison of drug loading of drug@MIL-100 samples produced *via* various methods

	Sample	Synthesis method	Drug loading (wt. %)	Drug loading (g/g of MOF)	Reference
5-Fluorouracil	5-FU@MIL-100_REC	Reconstruction encapsulation	35.5 wt.%	0.6	This work
	5-FU@MIL-100	Immersion into drug solution	66.0 wt.%	-	Thi *et al.* [15]
	5-FU@MIL-88		28.0 wt.%	-	
	5-FU@MIL-53		13.1 wt.%	-	
Caffeine	CAF@MIL-100_REC	Reconstruction encapsulation	64.7 wt.%	1.8	This work
	CAF@MIL-100	Immersion into drug solution	49.7 wt.%	-	Cunha *et al.* [16]
			24.2 wt.%	-	Horcajada *et al.* [17]
			52.4 wt.%	-	Márquez *et al.* [18]
Aspirin	ASP@MIL-100_REC	Reconstruction encapsulation	70.0 wt.%	2.3	This work
	ASP@MIL-100	Immersion into drug solution	24.8 wt.%	-	Rojas *et al.* [19]
			-	1.8	Singco *et al.* [20]
	ASP@MIL-127		-	0.14	Rojas *et al.* [21]

The drug loading was calculated from the TGA plots analysis *via* the formula:

$$\text{wt.}\,\% = \frac{m_{\text{loss (drug@MOF)}} - m_{\text{loss (MOF)}}}{m_{\text{loss (drug@MOF)}}}$$

where $m_{\text{loss (drug@MOF)}}$ is the weight loss of the drug@MOF systems and $m_{\text{loss (MOF)}}$ is the weight loss of the host MOF.

3.12. 5-Fluorouracil DFT calculations details

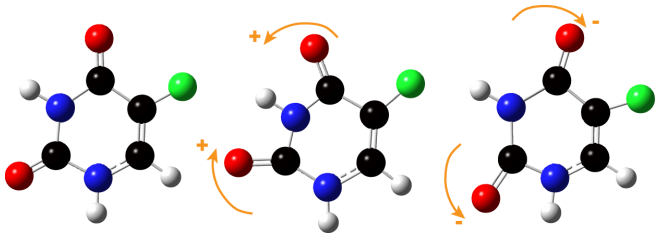

Figure S23. Illustration of the in-plane bending of OCNCO at ~12.3 THz (~410 cm^{-1}). Colour code: O in red, C in black, H in grey, N in navy blue, F in green.

3.13. Guest and host size comparison

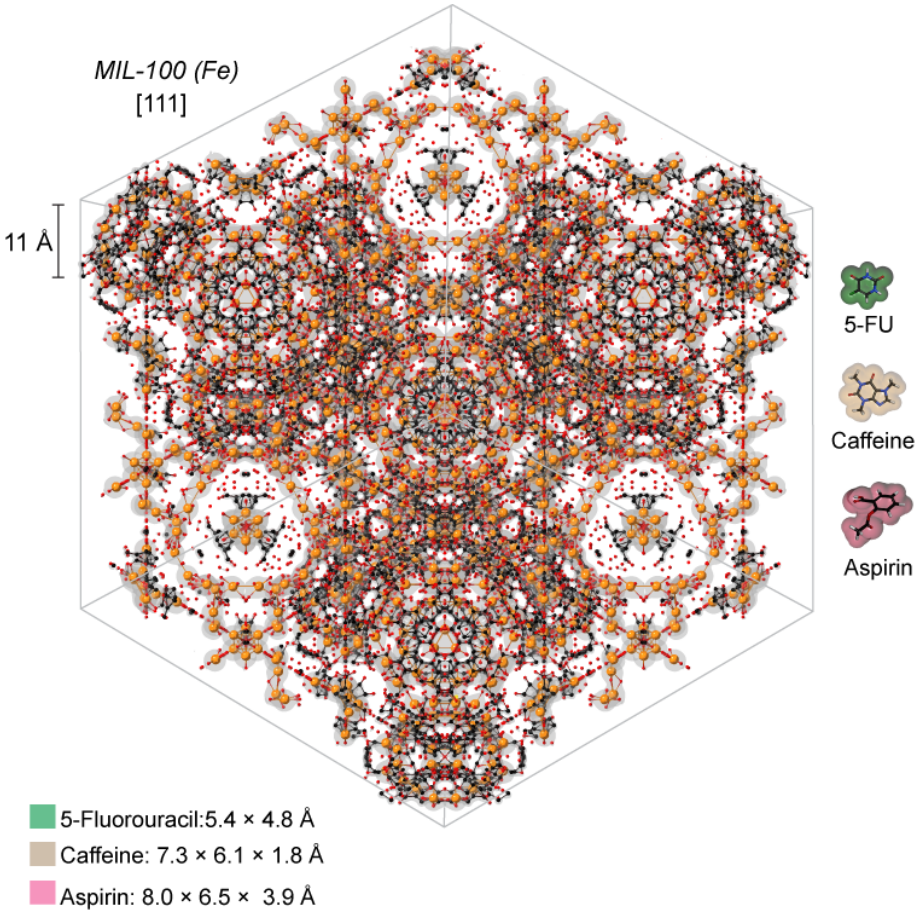

Figure S24. Schematic representation of host and guest molecular sizes. The comparison showcases how the mesocages of MIL-100 (Fe) can accommodate multiple of the chosen drug molecules within the MOF pores.

References

(1) Parker, S. F.; Fernandez-Alonso, F.; Ramirez-Cuesta, A. J.; Tomkinson, J.; Rudic, S.; Pinna, R. S.; Gorini, G.; Fernández Castañon, J., Recent and future developments on TOSCA at ISIS. *J. Phys.,* **2014,** *554*, 012003.
(2) Arnold, O.; Bilheux, J. C.; Borreguero, J. M.; Buts, A.; Campbell, S. I.; Chapon, L.; Doucet, M.; Draper, N.; Ferraz Leal, R.; Gigg, M. A.; Lynch, V. E.; Markvardsen, A.; Mikkelson, D. J.; Mikkelson, R. L.; Miller, R.; Palmen, K.; Parker, P.; Passos, G.; Perring, T. G.; Peterson, P. F.; Ren, S.; Reuter, M. A.; Savici, A. T.; Taylor, J. W.; Taylor, R. J.; Tolchenov, R.; Zhou, W.; Zikovsky, J., Mantid—Data analysis and visualization package for neutron scattering and SR experiments. *Nucl. Instrum. Meth. A,* **2014,** *764*, 156-166.
(3) Pinna, R. S.; Rudić, S.; Parker, S. F.; Armstrong, J.; Zanetti, M.; Škoro, G.; Waller, S. P.; Zacek, D.; Smith, C. A.; Capstick, M. J.; McPhail, D. J.; Pooley, D. E.; Howells, G. D.; Gorini, G.; Fernandez-Alonso, F., The neutron guide upgrade of the TOSCA spectrometer. *Nucl. Instrum. Meth. A,* **2018,** *896*, 68-74.
(4) M. J. Frisch, G. W. T., H. B. Schlegel, G. E. Scuseria, M. A. Robb, J. R. Cheeseman, G. Scalmani, V. Barone, G. A. Petersson, H. Nakatsuji, X. Li, M. Caricato, A. Marenich, J. Bloino, B. G. Janesko, R. Gomperts, B. Mennucci, H. P. Hratchian, J. V. Ortiz, A. F. Izmaylov, J. L. Sonnenberg, D. Williams-Young, F. Ding, F. Lipparini, F. Egidi, J. Goings, B. Peng, A. Petrone, T. Henderson, D. Ranasinghe, V. G. Zakrzewski, J. Gao, N. Rega, G. Zheng, W. Liang, M. Hada, M. Ehara, K. Toyota, R. Fukuda, J. Hasegawa, M. Ishida, T. Nakajima, Y. Honda, O. Kitao, H. Nakai, T. Vreven, K. Throssell, J. A. Montgomery, Jr., J. E. Peralta, F. Ogliaro, M. Bearpark, J. J. Heyd, E. Brothers, K. N. Kudin, V. N. Staroverov, T. Keith, R. Kobayashi, J. Normand, K. Raghavachari, A. Rendell, J. C. Burant, S. S. Iyengar, J. Tomasi, M. Cossi, J. M. Millam, M. Klene, C. Adamo, R. Cammi, J. W. Ochterski, R. L. Martin, K. Morokuma, O. Farkas, J. B. Foresman, and D. J. Fox, Gaussian 09, Revision A.02. *Gaussian, Inc.,* **2016,** (Wallingford CT).
(5) Dymkowski, K.; Parker, S. F.; Fernandez-Alonsob, F.; Mukhopadhyay, S., AbINS: The modern software for INS interpretation. *Phys. B Cond. Mat.,* **2018,** *551*, 443-448.
(6) Guillerm, V.; Ragon, F.; Dan-Hardi, M.; Devic, T.; Vishnuvarthan, M.; Campo, B.; Vimont, A.; Clet, G.; Yang, Q.; Maurin, G.; Ferey, G.; Vittadini, A.; Gross, S.; Serre, C., A series of isoreticular, highly stable, porous zirconium oxide based metal-organic frameworks. *Angew. Chem. Int. Ed.,* **2012,** *51* (37), 9267-71.
(7) Han, L.; Qi, H.; Zhang, D.; Ye, G.; Zhou, W.; Hou, C. M.; Xu, W.; Sun, Y. Y., A facile and green synthesis of MIL-100(Fe) with high-yield and its catalytic performance. *New J. Chem.,* **2017,** *41*, 13504-13509.
(8) Pilloni, M.; Padella, F.; Ennas, G.; Lai, S.; Bellusci, M.; Rombi, E.; Sini, F.; Pentimalli, M.; Delitala, C.; Scano, A.; Cabras, V.; Ferino, I., Liquid-assisted mechanochemical synthesis of an iron carboxylate Metal Organic Framework and its evaluation in diesel fuel desulfurization. *Microporous Mesoporous Mat.,* **2015,** *213*, 14-21.
(9) Samal, M.; Panda, J.; Biswal, B. P.; Sahu, R., Kitchen grinder: a tool for the synthesis of metal–organic frameworks towards size selective dye adsorption. *Cryst. Eng. Comm.* **2018,** *20*, 2486-2490.
(10) Zhang, F.; Shi, J.; Jin, Y.; Fu, Y.; Zhong, Y.; Zhu, W., Facile synthesis of MIL-100(Fe) under HF-free conditions and its application in the acetalization of aldehydes with diols. *Chem. Eng. J.,* **2015,** *259*, 183-190.
(11) Chen, G.; Leng, X.; Luo, J.; You, L.; Qu, C.; Dong, X.; Huang, H.; Yin, X.; Ni, J., In Vitro Toxicity Study of a Porous Iron(III) MetalOrganic Framework. *Molecules* **2019,** *24*, 1211.
(12) Zhang, X.; Shi, Q.; Shen, B.; Hu, Z.; Zhang, X., MIL-100(Fe) supported Mn-based catalyst and its behavior in Hg(0) removal from flue gas. *J. Hazard Mater.,* **2019,** *381*, 121003.
(13) Chaturvedi, G.; Kaur, A.; Umar, A.; Khan, M. A.; Algarni, H.; Kansal, S. K., Removal of fluoroquinolone drug, levofloxacin, from aqueous phase over iron based MOFs, MIL-100(Fe). *J. Solid State Chem.,* **2020,** *281*, 121029.
(14) Mahalakshmi, G.; Balachandran, V., FT-IR and FT-Raman spectra, normal coordinate analysis and ab initio computations of Trimesic acid. *Spectrochim. Acta A. Mol. Biomol. Spectrosc.,* **2014,** *124*, 535-47.
(15) Nguyễn Thị Hoài Phương, N. Đ. H., Investigation in Loading 5-Fluorouracil Ability of Iron-Organic Frameworks. *Vietnam J. Sci. Technol.,* **2018,** *56*, 219-227.
(16) Cunha, D.; Ben Yahia, M.; Hall, S.; Miller, S. R.; Chevreau, H.; Elkaïm, E.; Maurin, G.; Horcajada, P.; Serre, C., Rationale of Drug Encapsulation and Release from Biocompatible Porous Metal–Organic Frameworks. *Chem. Mater.,* **2013,** *25* , 2767-2776.
(17) Horcajada, P.; Chalati, T.; Serre, C.; Gillet, B.; Sebrie, C.; Baati, T.; Eubank, J. F.; Heurtaux, D.; Clayette, P.; Kreuz, C.; Chang, J. S.; Hwang, Y. K.; Marsaud, V.; Bories, P. N.; Cynober, L.; Gil, S.; Ferey, G.; Couvreur, P.; Gref, R., Porous metal-organic-framework nanoscale carriers as a potential platform for drug delivery and imaging. *Nat. Mater.,* **2010,** *9* , 172-8.
(18) Márquez, A. G.; Hidalgo, T.; Lana, H.; Cunha, D.; Blanco-Prieto, M. J.; Álvarez-Lorenzo, C.; Boissière, C.; Sánchez, C.; Serre, C.; Horcajada, P., Biocompatible polymer–metal–organic framework composite patches for cutaneous administration of cosmetic molecules. *J. Mater. Chem. B,* **2016,** *4* , 7031-7040.
(19) Rojas, S.; Colinet, I.; Cunha, D.; Hidalgo, T.; Salles, F.; Serre, C.; Guillou, N.; Horcajada, P., Toward Understanding Drug Incorporation and Delivery from Biocompatible Metal-Organic Frameworks in View of Cutaneous Administration. *ACS Omega,* **2018,** *3* , 2994-3003.
(20) Singco, B.; Liu, L.-H.; Chen, Y.-T.; Shih, Y.-H.; Huang, H.-Y.; Lin, C.-H., Approaches to drug delivery: Confinement of aspirin in MIL-100(Fe) and aspirin in the de novo synthesis of metal–organic frameworks. *Microporous Mesoporous Mat.,* **2016,** *223*, 254-260.
(21) Rojas, S.; Baati, T.; Njim, L.; Manchego, L.; Neffati, F.; Abdeljelil, N.; Saguem, S.; Serre, C.; Najjar, M. F.; Zakhama, A.; Horcajada, P., Metal-Organic Frameworks as Efficient Oral Detoxifying Agents. *J. Am. Chem. Soc.,* **2018,** *140* , 9581-9586.